

Quasi-antiferromagnetic multilayer stacks with 90 degree coupling mediated by thin Fe oxide spacers

G. Nagashima¹, Y. Kurokawa¹, Y. Zhong¹, S. Horiike¹, D. Schönke², P. Krautscheid², R. Reeve², M. Kläui², Y. Inagaki³, T. Kawae³, T. Tanaka¹, K. Matsuyama¹, K. Ohnishi⁴, T. Kimura⁴, and H. Yuasa^{1, a)}

¹ Faculty of Information Science and Electrical Engineering, Kyushu University, Fukuoka 819-0395, Japan

² Institute of Physics, Johannes Gutenberg-University Mainz, 55099 Mainz, Germany

³ Faculty of Engineering, Kyushu University, Fukuoka 819-0395, Japan

⁴ Faculty of Science, Kyushu University, Fukuoka 819-0395, Japan

Abstract

We fabricated quasi-antiferromagnetic (quasi-AFM) layers with alternating antiparallel magnetization in the neighboring domains via 90-deg magnetic coupling through an Fe-O layer. We investigated the magnetic properties and the relationship between the magnetic domain size and 90-deg magnetic coupling via experiments and calculations. Two types of samples with a Ru buffer and a (Ni₈₀Fe₂₀)Cr₄₀ buffer were prepared, and we found that with the NiFeCr buffer, the sample has a flatter Fe-O layer, leading to stronger 90-deg magnetic coupling and a smaller domain size compared with the Ru buffer sample. This trend is well explained by the bilinear and biquadratic coupling coefficients, A_{12} and B_{12} , in Landau–Lifshitz–Gilbert (LLG) simulations, suggesting the possibility of using both AFM and FM properties by controlling the quasi-AFM domain size.

a) Email: hiromi.yuasa@ed.kyushu-u.ac.jp

I. INTRODUCTION

Over the past decade, antiferromagnetic (AFM) spintronics received increasing attention due to the unique characteristics and potential of AFM materials as compared to ferromagnetic (FM) spintronics systems.¹⁻³ AFM materials exhibit alternating antiparallel magnetic moments with a resultant zero net magnetic moment, resulting in a state without dipolar interactions. From an application viewpoint, this lack of long range interactions is advantageous since stray fields can be neglected in the device design. AFM spintronics were first studied theoretically, with the prediction that a spin transfer torque (STT) could be obtained in AFM materials;^{1,4,5} later, experimental evidence of a STT in an AFM material was reported.⁶⁻⁹ Although spin torque induced oscillations (STOs) are theoretically expected in AFMs in the absence of a stray fields, strong STOs in AFM materials have not yet been directly observed because of the strong exchange coupling between adjacent atoms. Thus, to realize STOs in the absence of a stray field, we fabricated a quasi-AFM layer with domains of alternating antiparallel magnetization, resulting in a zero net global magnetization. The quasi-AFM layer exhibits FM coupling within one domain and AFM coupling between neighboring domains. Ultimately, if the domain size was reduced to the atomic scale, an AFM state would be obtained. In contrast, if the domains were enlarged to the sample size, an FM state would be achieved. This magnetic behavior is considered as a tunable intermediate state between FM and AFM materials.

The quasi-AFM layer was fabricated by 90-deg magnetic coupling, in which an interlayer exchange interaction occurs between two FM layers separated by a thin layer.¹⁰⁻²⁸ The magnetic coupling energy E can be expanded to a higher-order equation by considering the quadratic term, as follows:^{11, 13-28}

$$E = -A_{12} (\mathbf{M}_1 \cdot \mathbf{M}_2) - B_{12} (\mathbf{M}_1 \cdot \mathbf{M}_2)^2, \quad (1)$$

where \mathbf{M}_1 and \mathbf{M}_2 are the unit magnetization in the first and second FM layers and A_{12} and B_{12} are the bilinear and biquadratic coupling coefficients, respectively. When $|A_{12}| > 2|B_{12}|$, \mathbf{M}_1 and \mathbf{M}_2 are parallel (FM coupling) or antiparallel (AFM coupling). In contrast, when $|A_{12}| < 2|B_{12}|$ and $B_{12} < 0$, \mathbf{M}_1 and \mathbf{M}_2 take up an intermediate orientation between FM and AFM, exhibiting ± 90 -deg magnetization (90-deg magnetic coupling). A small $|A_{12}|$ and large $|B_{12}|$ are obtained when the FM and AFM coupling energies compete between \mathbf{M}_1 and \mathbf{M}_2 . This phenomenon was first observed experimentally in Fe/Cr/Fe(001)¹¹ and Fe/Cu/Fe(001)¹⁵ trilayers with a metallic spacer. Strong 90-deg magnetic coupling in two FM layers was later observed through a magnetic oxide layer.^{19–21} When the magnetization of the first FM layer is pinned by the exchange bias of an AFM layer, the second FM layer must exhibit domains with antiparallel magnetization due to the ± 90 -deg magnetic coupling energy and magnetostatic energy. Thus, a quasi-AFM layer can be obtained, where the magnetic domain size is expected to be determined by the 90-deg magnetic coupling energy. To design a quasi-AFM layer, the domain size must be controlled. Therefore, in this paper, the magnetic properties of a quasi-AFM layer fabricated by 90-deg magnetic coupling via an Fe-O layer were investigated, and the relationship between the magnetic domain structure and 90-deg magnetic coupling was investigated.

II. EXPERIMENTAL

Figure 1 shows the two sample structures employed in this work: (a) Ta 5 nm/Ru 2 nm/Ir₂₂Mn₇₈ 5 nm/Co₉₀Fe₁₀ (A) 2 nm/Fe-O 2 nm/Co₉₀Fe₁₀ (B) 2 nm/Cu 6 nm/Co₉₀Fe₁₀ (C) 2.5 nm/Cu 1 nm/Ta 5 nm and (b) Ta 5 nm/(Ni₈₀Fe₂₀)Cr₄₀ 5 nm/Co₉₀Fe₁₀ 1 nm/Ir₂₂Mn₇₈ 5 nm/Co₉₀Fe₁₀

(A) 2 nm/Fe-O 2 nm/Co₉₀Fe₁₀ (B) 2 nm/Cu 6 nm/Co₉₀Fe₁₀ (C) 2.5 nm/Cu 1 nm/Ta 5 nm. The samples were deposited on a thermally oxidized Si wafer in a DC magnetron sputtering system. As shown in Fig. 1(a) and (b), the samples differ only by the buffer layer, with either Ta/Ru or Ta/NiFeCr/CoFe buffers. Ta/Ru is a commonly used buffer for fcc stacked multilayer films, and the NiFeCr buffer is known to lead to a large grain size for the subsequently deposited film. The magnetization of CoFe (A) is pinned by the exchange bias from IrMn, and the magnetizations of CoFe (A) and CoFe (B) are coupled at ± 90 deg via the Fe-O layer. CoFe (C) is a free layer for magnetoresistance measurements. The Fe-O layer was fabricated by a natural oxidation process. After the deposition of Fe₃O₄, oxygen gas was introduced into the vacuum chamber. To establish an exchange biasing direction, the films were annealed in a field of 4.1 kOe at 270°C for 1 h.

A vibrating-sample magnetometer (VSM) and a superconducting quantum interference device (SQUID) were used to measure hysteresis loops at room temperature. The MR ratio was measured using a four-point probe, and the fine structure was investigated by cross-sectional transmission electron microscopy (TEM) analysis. Observations were performed using a JEM-ARM200F (Nihon Denshi) operating at 200 kV on specimens prepared by milling. The magnetic domain structure was studied by scanning electron microscopy with polarization analysis (SEMPA). SEMPA is a useful tool for determining the magnetization vector and for obtaining a 2D map with nanoscale resolution.^{28,29} Recent advances in time resolution also improved magnetic dynamics investigations.^{30,31} We prepared two model samples with a 2-nm Ta capping layer on the CoFe (B) layer for SEMPA. After the Ta capping layer was milled at a rate of 0.5 Å/min, which is sufficiently low to avoid damage, the magnetic domains of the CoFe (B) layer were observed.

III. CALCULATIONS

The magnetization dynamics were determined by solving the Landau–Lifshitz–Gilbert (LLG) equation. The effective field \mathbf{H}_{eff} in the LLG equation is the vector sum of the anisotropy field \mathbf{H}_{af} , exchange field \mathbf{H}_{ex} , static magnetic field \mathbf{H}_{st} , applied magnetic field \mathbf{H}_{app} , and bilinear and biquadratic exchange fields \mathbf{H}_{bl} and \mathbf{H}_{bq} . In two magnetic layers i and j with normalized magnetization \mathbf{m}_i and \mathbf{m}_j acting through a spacer, the bilinear and biquadratic exchange fields \mathbf{H}_{bl} and \mathbf{H}_{bq} are given by³²

$$\mathbf{H}_{bl,i} = \frac{A_{12}}{\mu_0 M_s d_i} \mathbf{m}_j(t)$$

and

$$\mathbf{H}_{bq,i} = \frac{2B_{12}}{\mu_0 M_s d_i} \begin{pmatrix} m_{i,x} m_{j,x}^2 + m_{j,x} (m_{i,y} m_{j,y} + m_{i,z} m_{j,z}) \\ m_{i,y} m_{j,y}^2 + m_{j,y} (m_{i,x} m_{j,x} + m_{i,z} m_{j,z}) \\ m_{i,z} m_{j,z}^2 + m_{j,z} (m_{i,y} m_{j,y} + m_{i,x} m_{j,x}) \end{pmatrix}$$

with $i \neq j$,

(2)

where A_{12} and B_{12} are the bilinear and biquadratic exchange coupling coefficients, respectively, M_s is the saturation magnetization, and d_i is the thickness of layer i .

Here, we consider the CoFe (A) 2 nm/Fe-O 2 nm/CoFe (B) 2 nm trilayer. In our model, the magnetic grain size is $10 \times 10 \times 2$ nm, and the sample has $560 \times 560 \times 3$ grains, as shown in Fig. 2. The anisotropy field was set to 35 Oe, and the saturation magnetization M_s , anisotropy field H_{af} , and Gilbert damping constant α for the Co₉₀Fe₁₀ layers were 1450 emu/cm³, 35 Oe, and 0.01, respectively. The exchange constant A was 1×10^{-6} erg/cm, and the gyromagnetic ratio γ was 1.76×10^7 Oe⁻¹s⁻¹. The calculation step dt was 10 fs. The pinned layer, CoFe (A), was evaluated by applying a bias magnetic field of 400 Oe. The magnetic field was applied to the films from -10000

to 10000 Oe parallel to the bias magnetic field, with a sweep time of 200 ns.

IV. RESULTS AND DISCUSSION

A. Magnetic properties

Figures 3(a) –(d) show MH and MR loops for the samples with Ru and NiFeCr buffer layers, respectively, for a magnetic field directed parallel (0 deg) and perpendicular (90 deg) to the exchange bias field. In this case the MH loop was obtained by VSM. The MH and MR loops under an applied field of 0 deg provide a reference for detecting the exchange bias field of IrMn. Figures 3(a) and (c) show that the exchange bias field of IrMn is 320 and 90 Oe for the Ru and NiFeCr buffer samples, respectively. Next, we focused on the MH and MR loops under a field applied at 90 deg, as shown in Fig. 3(b) and (d). Since this case is more complicated, the magnetization configuration is illustrated by schematic images of the magnetization orientation, as shown in Fig. 3(e). The states (i) –(iv) in Fig. 3(e) correspond to the states (i) –(iv) in Fig. 3(b) and (d). For state (i), the CoFe (A), (B), and (C) layers exhibit a magnetization parallel to the applied magnetic field. As the field decreases across zero from state (i) to (ii), the magnetization of CoFe (A) rotates to the exchange bias field direction. CoFe (A) and CoFe (B) are coupled, with an angle of ± 90 deg for state (ii). When the applied field is decreased further from state (ii) to (iii), the 90-deg coupling between CoFe (A) and CoFe (B) is broken, and consequently, the CoFe (A), (B), and (C) layers exhibit a magnetization parallel to the applied field, which is opposite to the direction for state (i). Because the MH and MR loops in Fig. 3(b) and (d) are symmetrical for a zero magnetic field, we conclude that 90-deg magnetic coupling was realized between CoFe (A) and (B) for the samples with Ru and NiFeCr buffer layers.

Here, we define H_{90} as the magnetic field at which the 90-deg magnetic coupling is broken.

As shown in Fig. 3(b) and (d), H_{90} is 50 and 100 Oe for the Ru and NiFeCr buffer samples, respectively. Thus, the 90-deg magnetic coupling energy of the sample with the NiFeCr buffer layer is larger than that for the Ru buffer layer.

B. Cross-sectional TEM observation

To investigate the origin of the difference in H_{90} for the samples with different buffer layers, high-resolution cross-sectional TEM images were acquired for the Ru and NiFeCr buffer layer samples, as shown in Fig. 4. Here we focus on the roughness of the Fe-O layer. Visual inspection shows that the NiFeCr buffer sample is significantly flatter than the Ru buffer sample. While the Ru buffer sample has a roughness of 2 nm, the NiFeCr buffer sample has a roughness of less than 0.2 nm, indicating that the roughness can be changed 10-fold by selecting an appropriate buffer layer. The Fe-O roughness is important for 90-deg magnetic coupling, which requires a balance between the FM and AFM coupling energies of CoFe (A) and (B) through the Fe-O layer. Typically, the roughness of a sputtered magnetic layer on a SiO₂ substrate depends on the columnar crystalline grains, which influence the FM coupling energy, also known as orange peel coupling.³³⁻

³⁶ The orange peel coupling energy J is given as

$$J = \frac{\pi^2}{\sqrt{2}} \frac{h^2}{\lambda} (\mu_0 M_1 M_2) \exp(-2\pi\sqrt{2}t_s / \lambda), \quad (3)$$

where h and λ are the amplitude and wavelength of the roughness, M_1 and M_2 are the magnetization of CoFe (A) and CoFe (B), respectively, and t_s is the thickness of the Fe-O layer. Based on Eq. (3), as the amplitude h increases, the orange peel coupling energy J increases. Therefore, a greater roughness leads to stronger FM coupling, and the balance between the FM and AFM coupling

energies is degraded. As a result, the 90-deg coupling becomes weak. For this reason, a flat Fe-O layer is important for achieving strong 90-deg magnetic coupling. From the viewpoint of flatness, the NiFeCr buffer is suitable due to its large columnar crystalline grains. It is known that the NiFeCr buffer increases the grain size, resulting in a flatter layer.³⁷ Our samples with Ru and NiFeCr buffers exhibited CoFe (A) grain sizes of approximately 15 and 50 nm, respectively, which we can identify as a cause of the observed difference in flatness. Thus, by choosing the appropriate buffer layer, we have a means to control the magnitude of 90-deg magnetic coupling.

C. Scanning electron microscopy with polarization analysis (SEMPA)

Although we can predict the macroscopic average magnetic direction of CoFe (B) from the MH and RH loops, as mentioned in Section A, the finescale domain structure is still unknown. To determine whether the CoFe (B) layer becomes a quasi-AFM layer, direct observation of the magnetic domain structures of CoFe (B) is necessary. Therefore, the CoFe (B) layers in the Ru and NiFeCr buffer samples were observed by high resolution SEMPA imaging. **Two model samples with a 2-nm Ta capping layer on the CoFe (B) layer were prepared. After the Ta capping layer was milled in chamber, the magnetic domains of the CoFe (B) layer were observed.** Topographic images are presented in Fig. 5(a) and (d), demonstrating that the CoFe (B) surface is smooth with no significant corrugations even after the Ta capping layer is milled. Thus, damage is not incurred during sample preparation. The in-plane magnetization M_x [Fig. 5(b), (e)] and M_y [Fig. 5(c), (f)] correspond to the parallel and perpendicular magnetization components with respect to the exchange bias field from IrMn, respectively. The white and black arrows in Fig. 5 denote the direction of the magnetization. For both samples, magnetic domains with antiparallel magnetization were observed, consistent with the expectation that the CoFe (B) layers became

quasi-AFM layers. However, differences were observed between the Ru and NiFeCr buffer samples. In Fig. 5(b) and (c), we can observe a difference in both M_y and M_x , indicating that the CoFe(B) layer in the Ru buffer sample has a magnetization that is tilted from the x axis, namely, the exchange biasing direction. This behavior is assumed to arise from the FM coupling caused by orange peel coupling, as mentioned above. In contrast, for the CoFe(B) layer in the NiFeCr buffer sample, no significant M_x component was observed, as shown in Fig. 5(e), indicating that the 90-deg magnetic coupling in the NiFeCr buffer sample is stronger than that of the Ru buffer sample. As shown in Fig. 5(c) and (f), the average magnetic domain size of the CoFe (B) layer in the Ru and NiFeCr buffer samples is 1 and 0.4 μm , respectively. Thus, the domain size in the Ru buffer sample is at least twice as large as that for the NiFeCr buffer sample. The magnetization and magnetic domain structure are determined when the total energy is minimized and are influenced by the static magnetic energy with respect to the total energy. The magnetization of CoFe (B) in the Ru buffer sample is tilted from the x axis due to weak 90-deg magnetic coupling, which leads to an increased magnetic domain size.

D. Magnetic domain structure determined by micromagnetic LLG simulation

To investigate the relationship between the magnetic domain structure and the magnitude of the 90-deg magnetic coupling, micromagnetic LLG simulations were performed. As mentioned in the introduction, 90-deg magnetic coupling depends on the sign and magnitude of the interlayer coupling coefficients A_{12} and B_{12} , which can be estimated from fits of the experimental data while noting the following: the magnetic field at which the magnetic moments of the CoFe (B) layer begin to deviate from the applied field direction and the magnitude of the magnetic field at the magnetization reversal. The coefficient A_{12} denotes the magnitude of the magnetization jump, and

B_{12} denotes the magnitude of the magnetization rotation. Figure 6(a) presents MH curves simulated by changing B_{12} from -0.2 to -0.05 mJ/m² with A_{12} fixed at 0 mJ/m². When a field is swept from a negative value ($-x$) to zero, the magnetization of the CoFe (B) layer rotates by ± 90 deg with respect to the magnetization of CoFe (C). As the field is increased from zero to a positive value ($+x$), the magnetization of CoFe (C) reverses to the direction of the applied field at the exchange bias field of IrMn. Then, the magnetization of CoFe (B) gradually rotates to the applied field ($+x$) and finally saturates. As shown in Fig. 6(a), while the magnitude of the magnetization jump does not depend on B_{12} , the slope of the magnetization rotation does depend on B_{12} . When the magnitude of B_{12} is large, rotating the magnetization of CoFe (B) to the applied field is difficult; thus, a larger magnitude of B_{12} leads to stronger 90-deg coupling. Figure 6 (b) shows MH curves simulated by changing A_{12} from 0 to 0.2 mJ/m² with B_{12} fixed at -0.2 mJ/m². While the slope of magnetization rotation is not influenced by A_{12} , the magnitude of the magnetization jump does depend on the value of A_{12} . When the magnitude of A_{12} is large, the magnetization jump is large. Schematic images of the magnetization for states of (c)–(h) in Fig. 6(b) are shown in Fig. 6(c)–(h). The average magnetization of states of (c)–(e) and (f)–(h) is $+x$ and $-x$, respectively, and the angle between the magnetization of CoFe (B) and CoFe (C) is 90, 76, and 60 deg for A_{12} values of 0, 0.1, and 0.2 mJ/m², respectively. Thus, the magnitude of the magnetization jump is determined by the angle between the magnetization of CoFe (B) and CoFe (C) in a zero or near-zero magnetic field.

To derive the bilinear and biquadratic coupling coefficients A_{12} and B_{12} , we fitted the MH curves of the (a) Ru and (b) NiFeCr buffer samples for a field of -10 to 10 kOe applied parallel to the exchange bias field. In Fig. 7, the black dots show the experimental data measured by the SQUID instrument. Since the MH curve measured for the positive field contains the magnetization motion in both CoFe (A) and CoFe (B), the MH curve for the negative field was used for fitting.

For the calculated MH curve, A_{12} and B_{12} were independently varied from 0 to 1.0 mJ/m² and from -0.6 to -0.1 mJ/m² by 0.1 mJ/m², respectively. In Fig. 6, the red and blue lines represent the MH curves given by the LLG equation for the (a) Ru and (b) NiFeCr buffer samples, respectively. As shown in Fig. 7(a), the A_{12} and B_{12} values for the Ru buffer sample are 0.4 and -0.3 mJ/m², respectively, based on MH curve fitting. In the same manner, the A_{12} and B_{12} values for the NiFeCr buffer sample are estimated as 0.6 and -0.6 mJ/m², as shown in Fig. 7(b).

The obtained A_{12} and B_{12} values were plotted in a magnetic coupling map, as shown in Fig. 8.²⁴ Both the Ru (red circle) and NiFeCr (blue circle) buffer samples exhibit 90-deg magnetic coupling component as well as ferromagnetic coupling component. The Ru and NiFeCr buffer samples display angles of 40 and 60 deg between CoFe (B) and CoFe (C), respectively, in agreement with the SEMPA images, where an x magnetization component is clearly observed in the Ru buffer sample. Additionally, previously reported values for metallic spacers such as Au, Al, and Cu are plotted as small black circles, and that for an NiO spacer is plotted as a small open circle.^{13-15, 18} These metallic spacers exhibit a smaller biquadratic coupling coefficient B_{12} than the magnetic oxide spacer.

Under these conditions for A_{12} and B_{12} , the magnetic domain structure of the CoFe (B) layer was calculated using the LLG equation. Figure 9 shows the calculated domain structures for the (a) Ru and (b) NiFeCr buffer samples. The CoFe (B) layers in both samples exhibit magnetic domains of roughly antiparallel magnetization with respect to the neighboring domains, and the magnetic domain size of the Ru buffer sample is twice as large as that of the NiFeCr buffer sample, in agreement with the experimental results presented in Fig. 5 for SEMPA. This agreement between the simulated and experimentally observed domain structures indicates that the domain size of the quasi-AFM layer can be controlled by changing the 90-deg magnetic coupling in

conventional magnetic materials such as CoFe with a convenient thickness. By changing the domain size from the atomic scale to the sample size, the quasi-AFM layer transforms from the AFM state to the FM state. Domain size control is important for STO observations in devices without stray fields. Moreover, the collinear magnetic materials Mn and Cr were reported to exhibit large values of B_{12} at -1.5 and -4 mJ/m², respectively.^{17, 20} Thus, the domain size of a quasi-AFM layer can potentially be reduced by 90-deg coupling with a large biquadratic coupling coefficient B_{12} .

V. CONCLUSION

We have successfully fabricated a quasi-AFM layer by 90-deg magnetic coupling through an Fe-O layer. We controlled the magnetic domain size by using two different buffer layers, Ru and NiFeCr, leading to different Fe-O roughness values. By fitting the MH curves, the bilinear and biquadratic coupling coefficients A_{12} and B_{12} were estimated. LLG simulations based on these coefficients accurately elucidated the magnetic domain structure of the quasi-AFM layers directly observed by SEMPA, indicating that the domain size can be controlled by altering the 90-deg magnetic coupling. This domain size can be tailored thus suggesting that quasi-AFM layers may potentially exhibit a spin torque between FM and AFM states without any stray fields.

ACKNOWLEDGMENTS

This work was supported by the Canon Foundation, the JSPS Program for Fostering Globally Talented Researchers, and JSPS KAKENHI Grant Number JP19K04471 as well as the German Research Foundation (DFG SFB TRR173 Spin+X).

REFERENCES

- ¹A. H. MacDonald and M. Tsoi, *Phil. Trans. R. Soc. A* **369**, 3098 (2011).
- ²Rembert Duine *Nature Mater.* **10**, 344 (2011).
- ³T. Jungwirth, X. Marti, P. Wadley, and J. Wunderlich, *Nature Nanotechnology* **11**, 231 (2016).
- ⁴A. S. Núñez, R. A. Duine, P. Haney, and A. H. MacDonald, *Phys. Rev. B* **73**, 214426 (2006).
- ⁵P. M. Haney and A. H. MacDonald, *Phys. Rev. Lett.* **100**, 196801 (2008).
- ⁶Z. Wei, A. Sharma, A. S. Nunez, P. M. Haney, R. A. Duine, J. Bass, A. H. MacDonald, and M. Tsoi, *Phys. Rev. Lett.* **98**, 116603 (2007).
- ⁷S. Urazhdin and N. Anthony, *Phys. Rev. Lett.* **99**, 046602 (2007).
- ⁸Z. Wei, J. Basset, A. Sharma, J. Bass, and M. Tsoi, *J. Appl. Phys.* **105**, 07D108 (2009).
- ⁹T. Moriyama, S. Takei, M. Nagata, Y. Yoshimura, N. Matsuzaki, T. Terashima, Y. Tserkovnyak, and T. Ono, *Appl. Phys. Lett.* **106**, 162406 (2015).
- ¹⁰M. Ruhrig, R. Schafer, A. Hubert, R. Mosler, J. A. Wolf, S. Demokritov, and P. Grünberg, *Phys. Status. Solidi. (a)* **125**, 635 (1991).
- ¹¹B. Heinrich, J. F. Cochran, M. Kowalewski, J. Kirschner, Z. Celinski, A. S. Arrott, and K. Myrtle, *Phys. Rev. B* **44**, 9348 (1991).
- ¹²J. Unguris, R. J. Celotta, and D. T. Pierce, *Phys. Rev. Lett.* **67**, 140 (1991).
- ¹³A. Fuss, S. Demokritov, P. Grünberg, and W. Zinn, *J. Magn. Magn. Mater.* **103**, L221 (1992).
- ¹⁴C. J. Gutierrez, J. J. Krebs, M. E. Flipkowski, and G. A. Prinz, *J. Magn. Magn. Mater.* **116**, L305 (1992).

- ¹⁵B. Heinrich, Z. Celinski, J. F. Cochran, A. S. Arrott, K. Myrtle, and S. T. Purcell, Phys. Rev. B **47**, 5077 (1993).
- ¹⁶B. Rodmacq, K. Dumesnil, P. Mangin, M. Hennion, Phys. Rev. B **48**, 3556 (1993).
- ¹⁷M. E. Filipkowski, J. J. Krebs, G. A. Prinz, and C. J. Gutierrez, Phys. Rev. Lett. **75**, 1847 (1995).
- ¹⁸P. A. A. van der Heijden, C. H. W. Swüste, W. J. M. de Jonge, J. M. Gaines, J. T. W. M. van Eemeren, and K. M. Schep, Phys. Rev. Lett. **82**, 1020 (1999).
- ¹⁹S.-S. Yana and P. Grünberg, and L.-M. Mei, J. Appl. Phys. **88**, 983 (2000).
- ²⁰H. Wang, A. Sato, K. Saito, S. Mitani, K. Takanashi, and K. Yakushiji, Appl. Phys. Lett. **90**, 142510 (2007).
- ²¹J. C. Slonczewski, Phys. Rev. Lett. **67**, 3172 (1991).
- ²²J. C. Slonczewski, J. Appl. Phys. **73**, 5957 (1993).
- ²³J. C. Slonczewski, J. Magn. Magn. Mater. **150**, 13 (1995).
- ²⁴S. O. Demokritov, J. Phys. D: Appl. Phys. **31**, 925 (1998).
- ²⁵H. Fukuzawa, K. Koi, H. Tomita, H. N. Fuke, H. Iwasaki, and M. Sahashi, J. Appl. Phys. **91**, 6684 (2002).
- ²⁶S. Maat, and B. A. Gurney, J. Appl. Phys. **93**, 7229 (2003).
- ²⁷C. H. Lai, and K. H. Lu, J. Appl. Phys. **93**, 8412 (2003).
- ²⁸K. Koike, H. Matsuyama, H. Todokoro, and K. Hayakawa, Jpn. J. Appl. Phys. **24**, 1078 (1985).
- ²⁹S. Unguris, G. G. Hembree, R. J. Celotta, and D. T. Pierce, J. Magn. Magn. Mater. **54**, 1629 (1986).
- ³⁰D. Schönke, A. Oelsner, P. Krautscheid, R. M. Reeve, and M. Kläui, Review of Scientific Instruments **89**, 083703 (2018).
- ³¹P. Krautscheid, R. M. Reeve, D. Schönke, I. Boverter, A. Conca, A. V. Chumak, B. Hillebrands,

J. Ehrler, J. Osten, J. Fassbender, and M. Kläui, Phys. Rev. B **98**, 214406 (2018).

³²M. Belmeguenai, T. Martin, G. Woltersdorf, M. Maier, and G. Bayreuther, Phys. Rev. B **76**, 104414 (2007).

³³J. C. S. Kools, W. K. Mauri, and T. Lin, J. Appl. Phys. **85**, 4466 (1999).

³⁴B. D. Schrag, A. Anguelouch, S. Ingvarsson, G. X. Y. Lu, P. L. Trouilloud, A. Gupta, R. A. Wanner, W. J. Gallagher, P. M. Rice, and S. S. P. Parkin, Appl. Phys. Lett. **77**, 2373 (2000).

³⁵D. Wang, J. M. Daughton, Z. Qian, C. Nordman, M. Tondra, and A. Pohm, J. Appl. Phys. **93**, 8558 (2003).

³⁶F. A. Shah, V. K. Sankar, P. Li, G. Csaba, E. Chen, and G. H. Bernstein, J. Appl. Phys. **115**, 17B902-1 (2014).

³⁷J. R. Childress, M. J. Carey, R. J. Wilson, N. Smith, C. Tsang, M. K. Ho, K. Carey, S. A. MacDonald, L. M. Ingall, B. A. Gurney, IEEE Trans. Magn. **37**, 1745 (2001).

FIGURE CAPTIONS

FIG. 1. Schematic film structures of samples with (a) Ru and (b) NiFeCr buffer layers.

FIG. 2. Schematic image of the simulation model. The model is discretized into cubic grains with dimensions of $10 \times 10 \times 2$ nm.

FIG. 3. MH and MR loops of samples with a Ru buffer layer (a)(b) and a NiFeCr buffer layer (c)(d). Magnetic fields were applied at 0 deg (a)(c) and 90 deg (b)(d) with respect to the exchange bias field. (e) Schematic images of the magnetization in the CoFe (A), (B), and (C) layers, where

the red and black arrows denote the magnetization and the applied magnetic field. The states of (i)–(iv) in (e) correspond to (i)–(iv) in (b)(d).

FIG. 4. High-resolution cross-sectional TEM images of samples with (a)(b) Ru and (c)(d) NiFeCr buffer layers. (a)(c) and (b)(d) present images with 500,000X and 2,000,000X magnification, respectively. The layer compositions are indicated.

FIG. 5. SEMPA images of samples with Ru (a)–(c) and NiFeCr (d)–(f) buffer layers. Topographic images of these samples are shown in (a) and (d). M_x (b)(e) and M_y (c)(f) are the x and y components of the in-plane magnetization, respectively. The white (black) arrows indicate magnetization directed toward the top or right (bottom or left).

FIG. 6. MH curves simulated by varying B_{12} from -0.2 to -0.05 mJ/m² with A_{12} fixed at 0 mJ/m² (a) and by varying A_{12} from 0 to 0.2 mJ/m² with B_{12} fixed at -0.2 mJ/m² (b). (c)–(h) present schematics of the magnetization for states (c)–(h) indicated in (b).

FIG. 7. MH curves for (a) Ru and (b) NiFeCr buffer samples with an applied field of -10 to 10 kOe at 0 deg. The black lines present data measured by the SQUID system. The red and blue lines present data calculated from the LLG equation. The insets display results from -1 to 1 kOe.

FIG. 8. A magnetic coupling map obtained from the bilinear and biquadratic coupling coefficients, A_{12} and B_{12} .²⁴ The blue and gray regions indicate stable FM and AFM coupling states, respectively. The pink region represents the intermediate state between FM and AFM coupling, including

This is the author's peer reviewed, accepted manuscript. However, the online version of record will be different from this version once it has been copyedited and typeset.

PLEASE CITE THIS ARTICLE AS DOI: 10.1063/1.5117869

complete 90-deg coupling. The results for the Ru and NiFeCr buffer samples are indicated by red and blue circles, respectively. The black and white circles present previously reported results for nonmagnetic metal spacers and a NiO spacer, respectively.^{13-15, 18}

FIG. 9. Calculated magnetic domain structures of (a) Ru and (b) NiFeCr buffer samples with dimensions of $5.6 \mu\text{m} \times 5.6 \mu\text{m} \times 6 \text{nm}$.

This is the author's peer reviewed, accepted manuscript. However, the online version of record will be different from this version once it has been copyedited and typeset.
PLEASE CITE THIS ARTICLE AS DOI: 10.1063/1.5117869

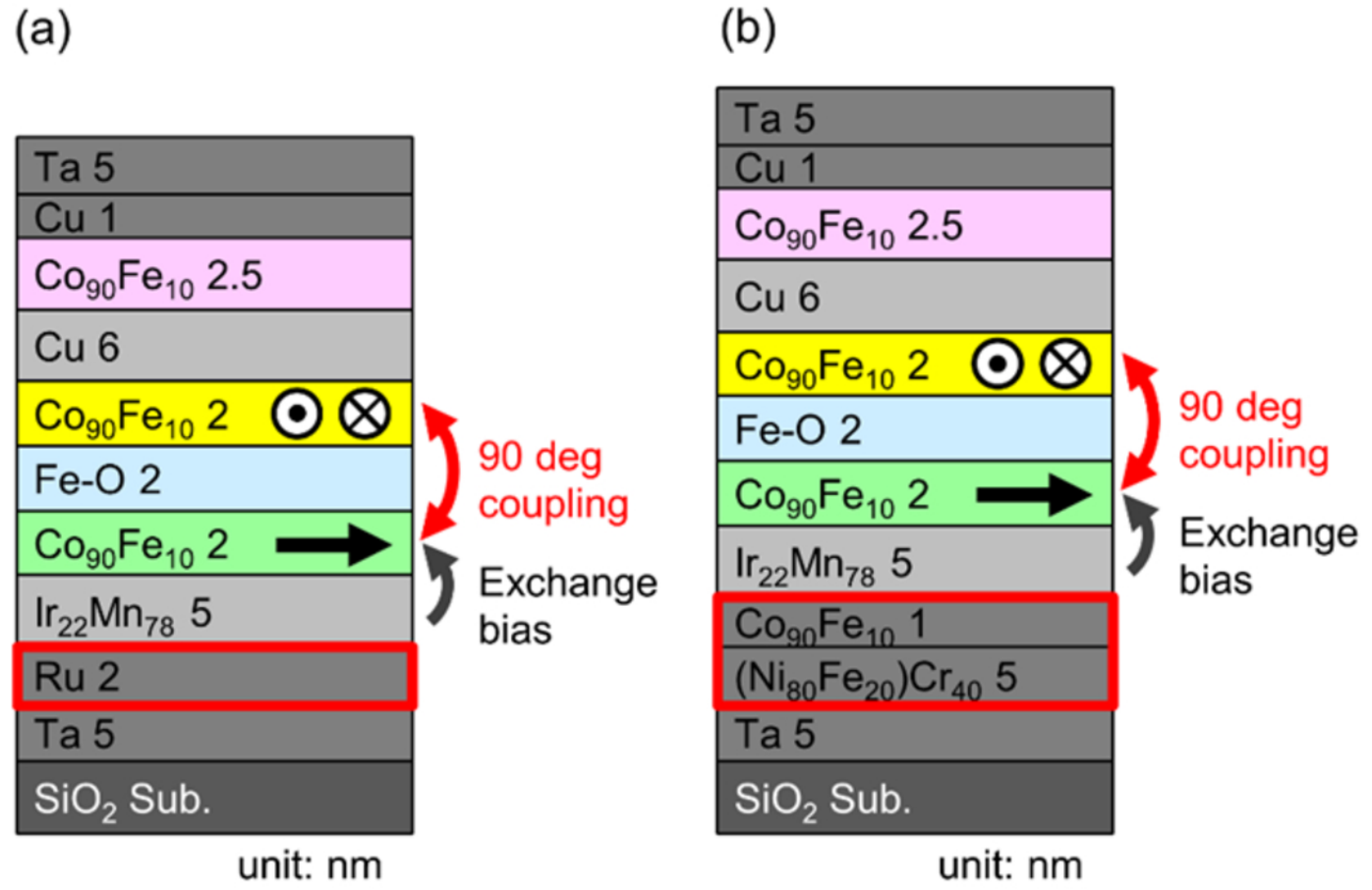


Fig. 1

This is the author's peer reviewed, accepted manuscript. However, the online version of record will be different from this version once it has been copyedited and typeset.
PLEASE CITE THIS ARTICLE AS DOI: 10.1063/1.5117869

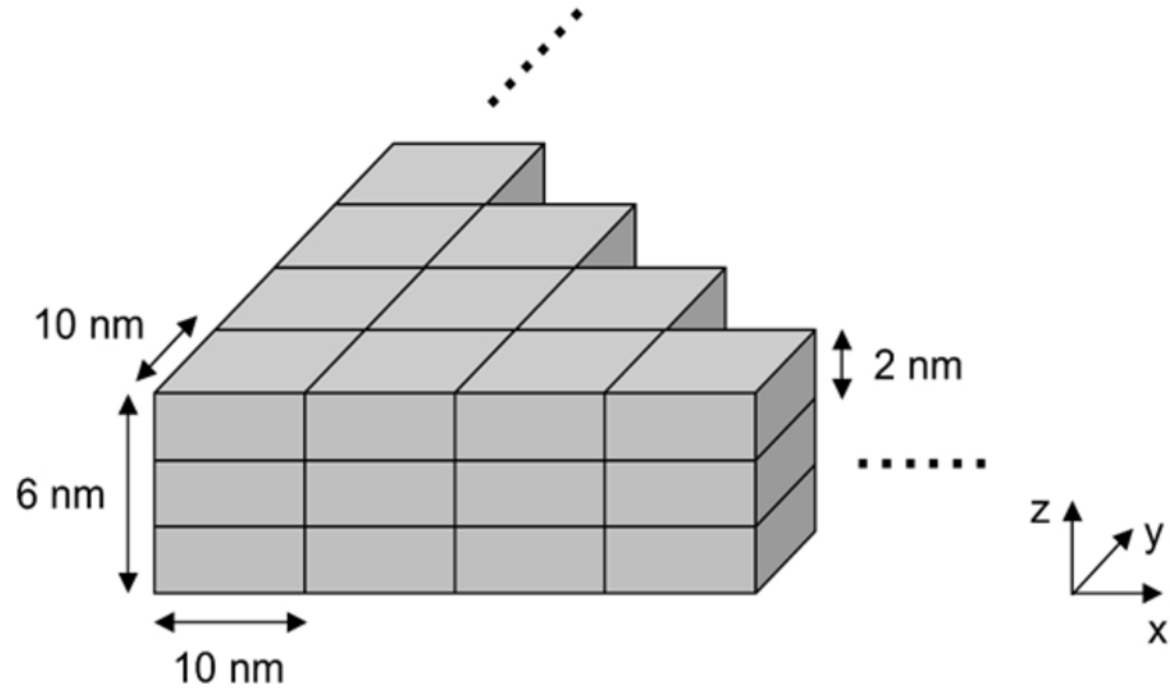


Fig. 2

This is the author's peer reviewed, accepted manuscript. However, the online version of record will be different from this version once it has been copyedited and typeset.
PLEASE CITE THIS ARTICLE AS DOI: 10.1063/1.5117869

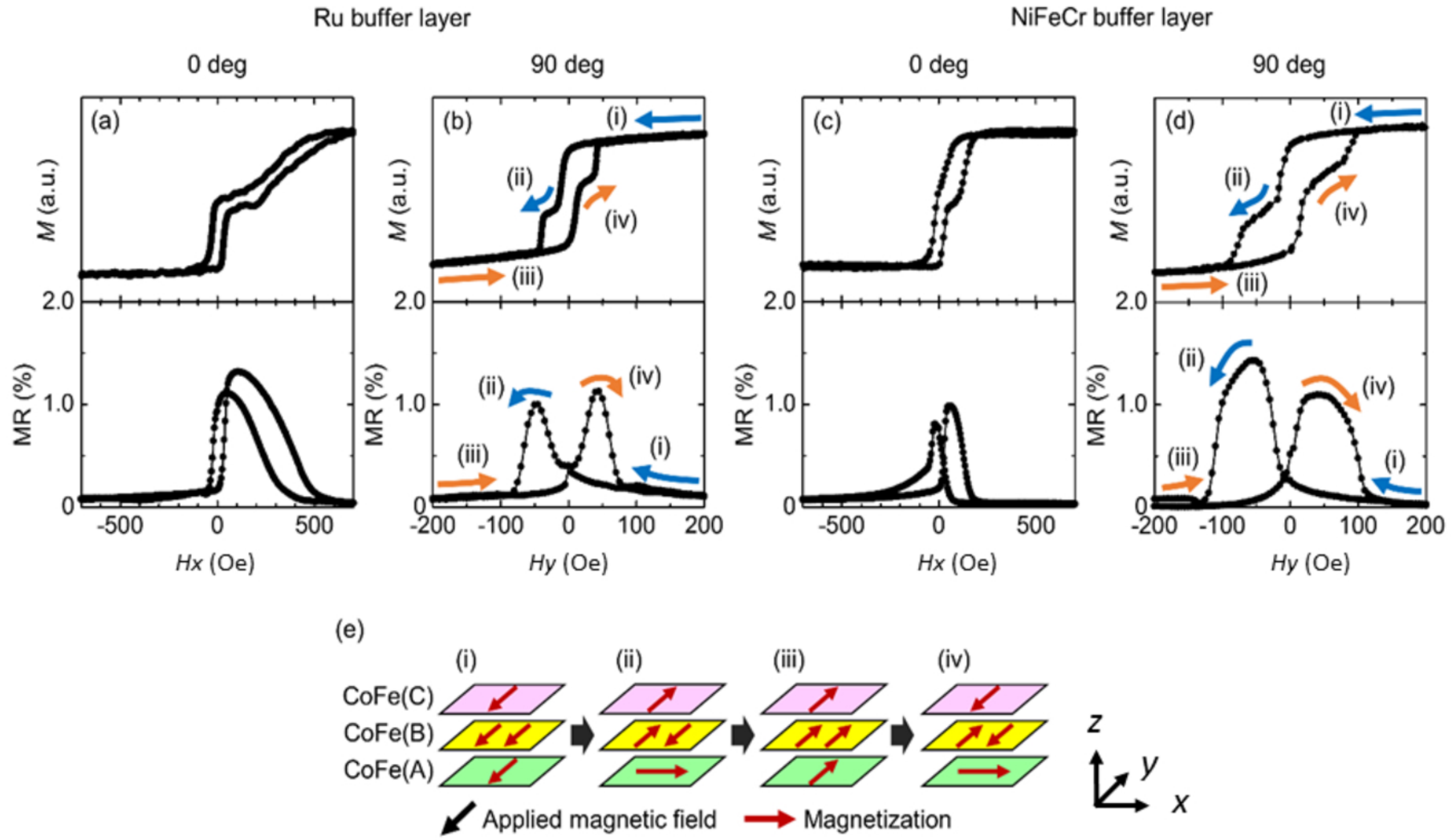
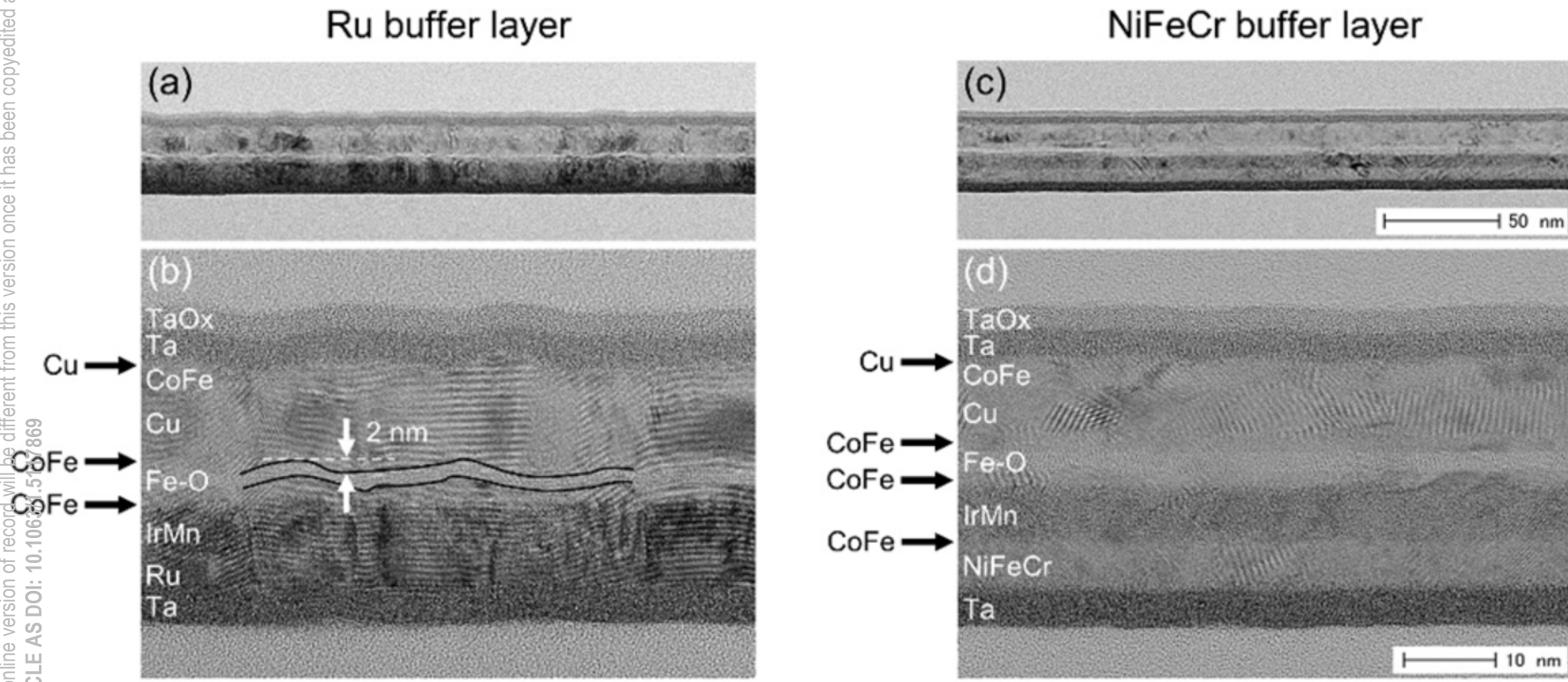


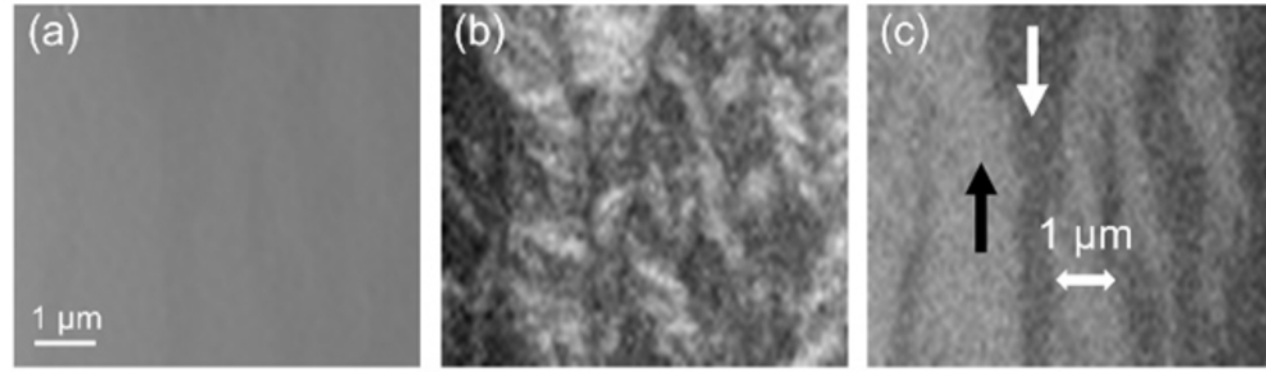
Fig. 3

This is the author's peer reviewed, accepted manuscript. However, the online version of record will be different from this version once it has been copyedited and typeset.
PLEASE CITE THIS ARTICLE AS DOI: 10.1063/1.517869

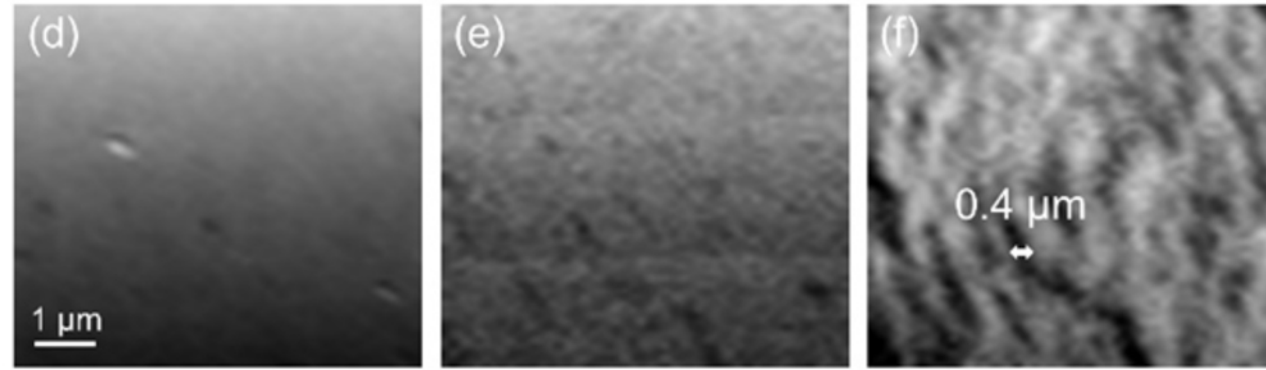


This is the author's peer reviewed, accepted manuscript. However, the online version of record will be different from this version once it has been copyedited and typeset.
PLEASE CITE THIS ARTICLE AS DOI: 10.1063/1.5117869

Ru buffer layer



NiFeCr buffer layer



Topography

 M_x  M_y

Fig. 5

This is the author's peer reviewed, accepted manuscript. However, the online version of record will be different from this version once it has been copyedited and typeset.
PLEASE CITE THIS ARTICLE AS DOI: 10.1063/1.5117869

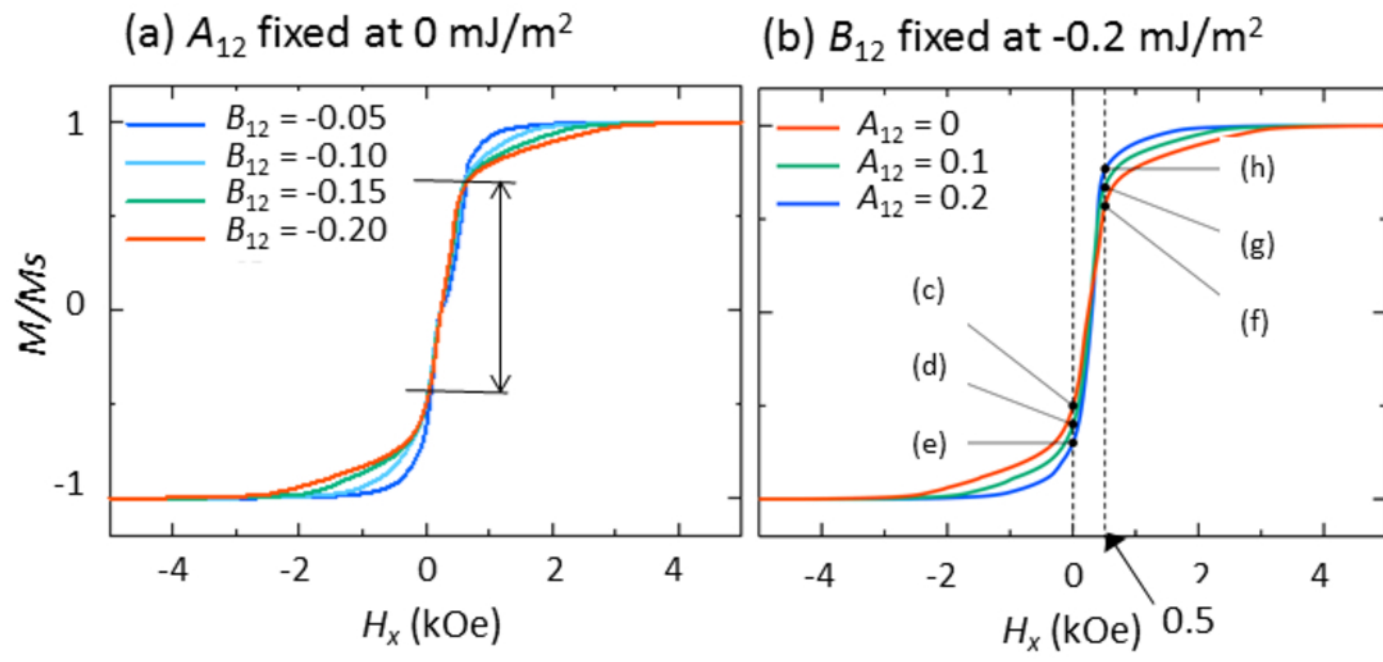


Fig. 6-1

This is the author's peer reviewed, accepted manuscript. However, the online version of record will be different from this version once it has been copyedited and typeset.
PLEASE CITE THIS ARTICLE AS DOI: 10.1063/1.5117869

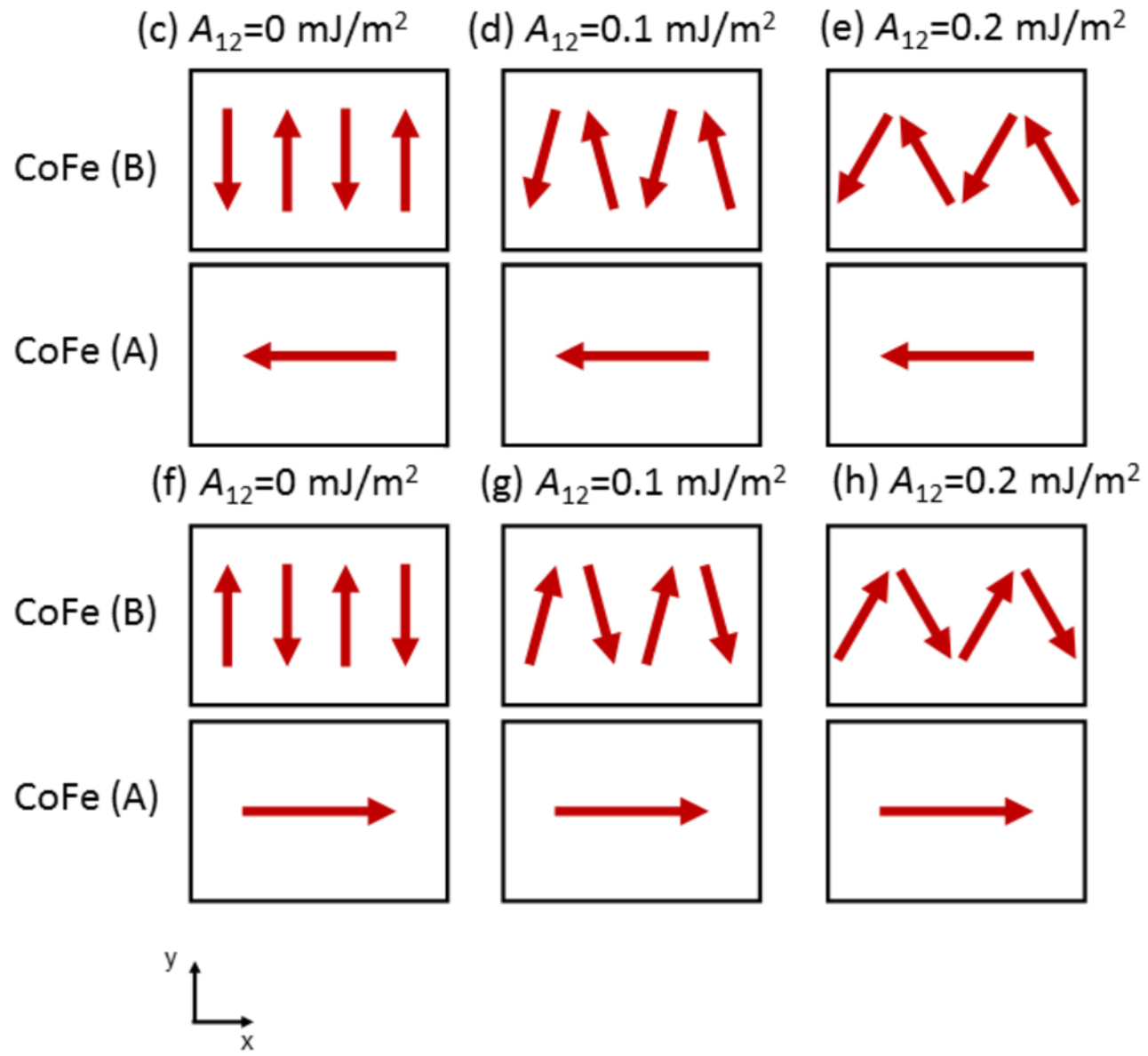


Fig. 6-2

This is the author's peer reviewed, accepted manuscript. However, the online version of record will be different from this version once it has been copyedited and typeset.
PLEASE CITE THIS ARTICLE AS DOI: 10.1063/1.5117869

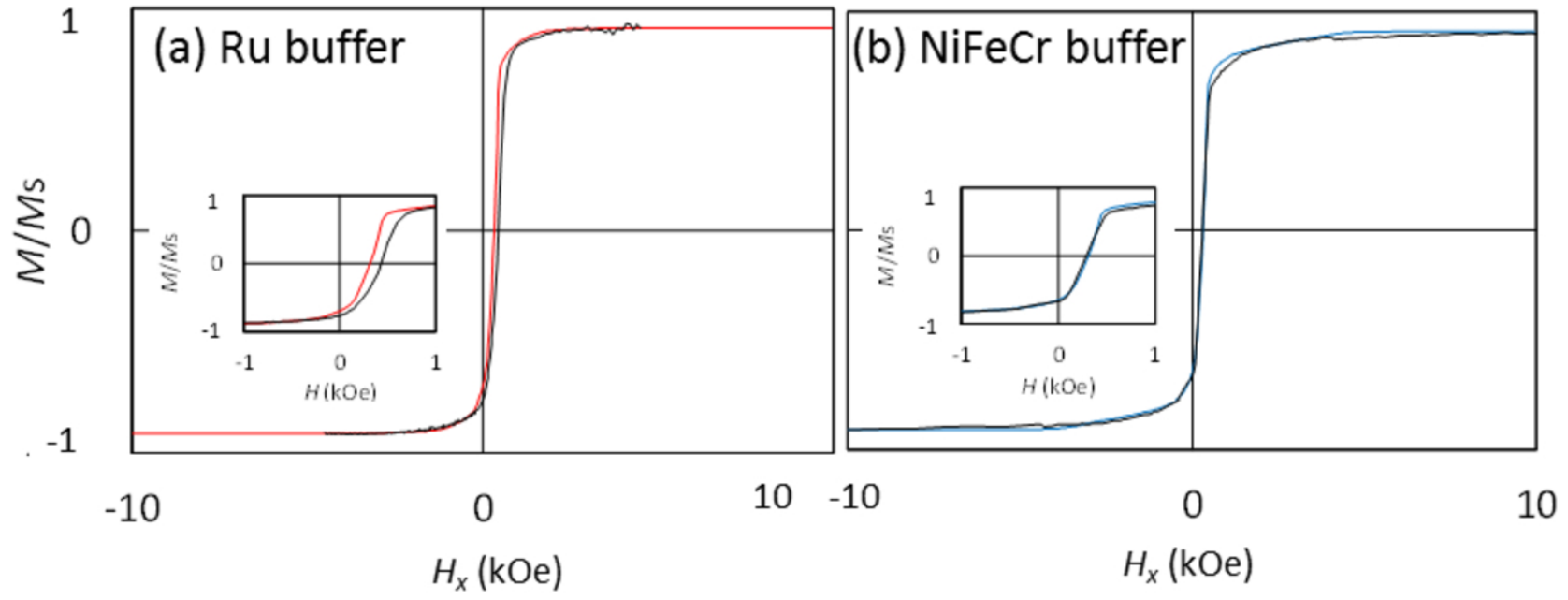


Fig. 7

This is the author's peer reviewed, accepted manuscript. However, the online version of record will be different from this version once it has been copyedited and typeset.
PLEASE CITE THIS ARTICLE AS DOI: 10.1063/1.5117869

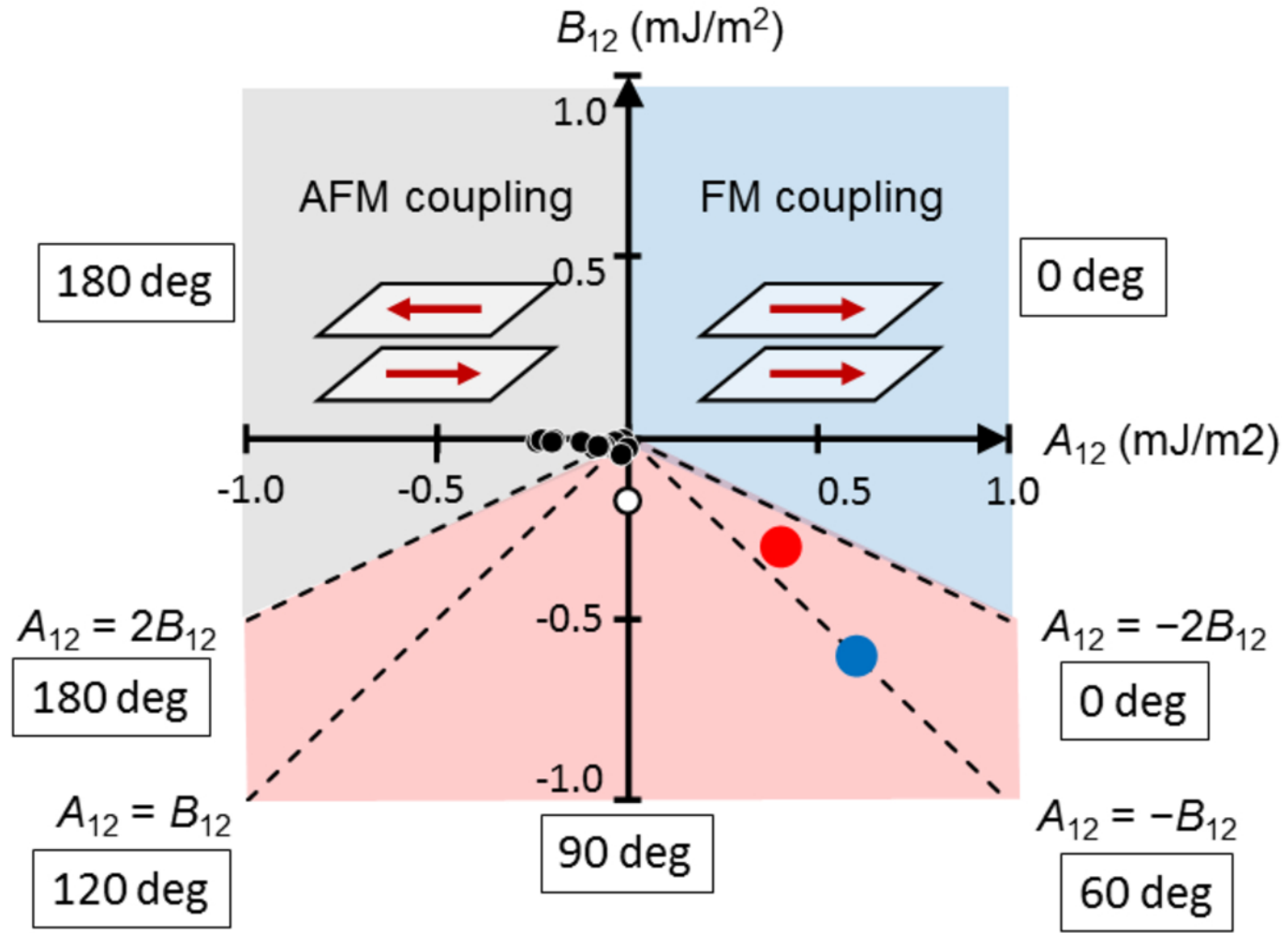
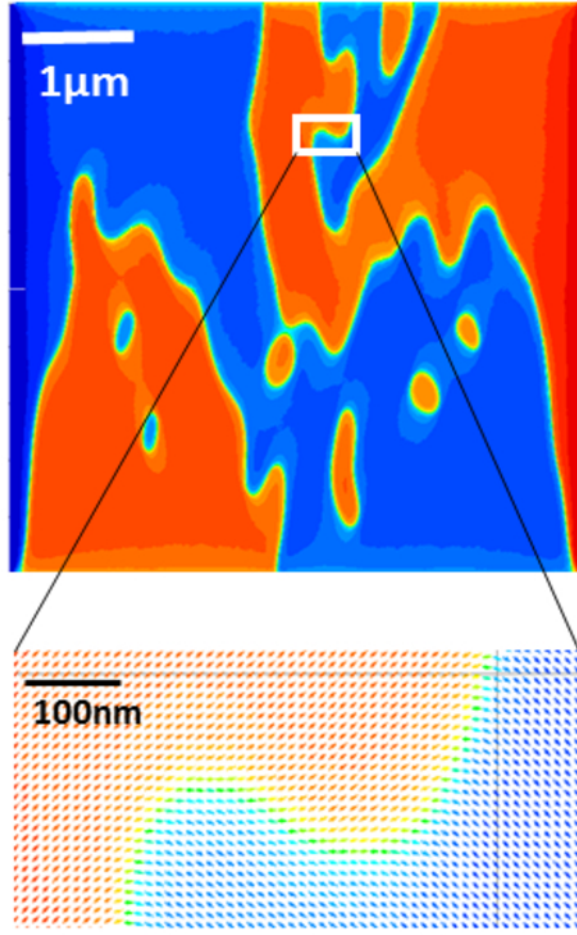


Fig. 8

This is the author's peer reviewed, accepted manuscript. However, the online version of record will be different from this version once it has been copyedited and typeset.
PLEASE CITE THIS ARTICLE AS DOI: 10.1063/1.5117869

(a) Ru buffer



(b) NiFeCr buffer

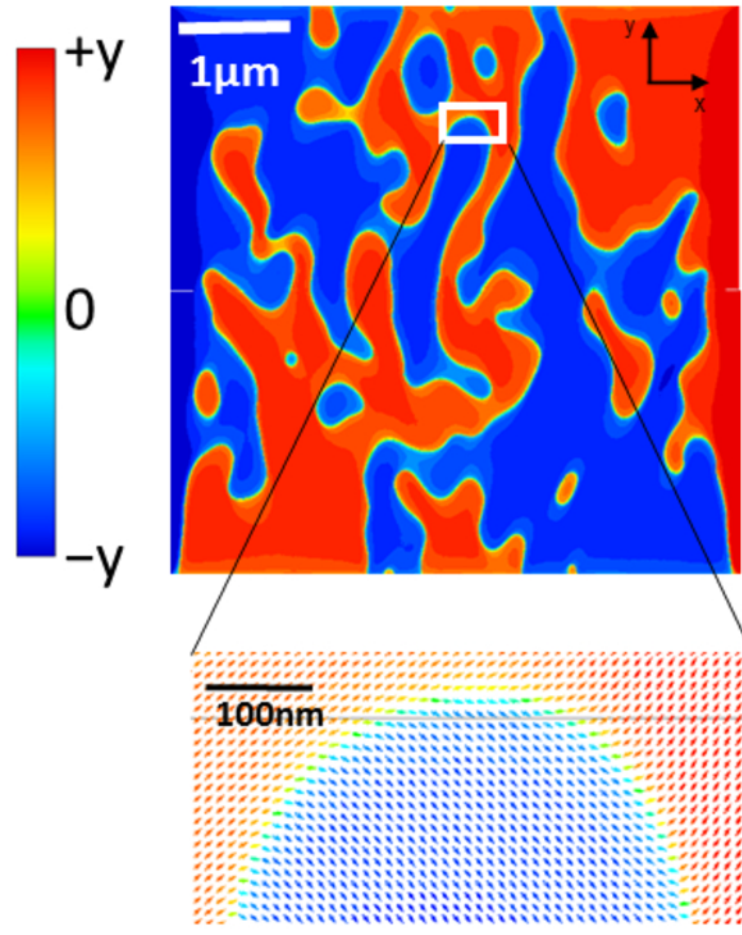


Fig. 9